Imaging of high-Q cavity optical modes by electron energy-loss microscopy

N. Le Thomas,[1,*,†] D. T. L. Alexander,[2] M. Cantoni,[2] W. Sigle,[3] R. Houdré,[1] and C. Hébert[2,4]

[1]*Institut de Physique de la Matière Condensée, École Polytechnique Fédérale de Lausanne (EPFL), Station 3, CH-1015 Lausanne, Switzerland*

[2]*Centre Interdisciplinaire de Microscopie Électronique (CIME), École Polytechnique Fédérale de Lausanne (EPFL), Station 12, CH-1015 Lausanne, Switzerland*

[3]*Max Planck Institute for Intelligent Systems, D-70569 Stuttgart, Germany*

[4]*Laboratoire de Spectrométrie et Microscopie Électronique (LSME), École Polytechnique Fédérale de Lausanne (EPFL), Station 12, CH-1015 Lausanne, Switzerland*

(Received 24 January 2013; published 29 April 2013)

We show a technique that images the intensity distribution and local state of polarization of the optical field of high-quality factor optical modes confined in dielectric planar photonic crystal nanocavities. Based on energy-loss spectroscopy of swift electrons, the technique gives a spatial resolution improved by a factor of 30 compared to the optical diffraction limit. Moreover, because the energy loss is induced by coupling of the moving charges with the local density of states of the dielectric cavity, it is sensitive to the entire volume of the confined electric field, not just its evanescent contributions. This three-dimensional sensitivity paves the way for a highly resolved tomography of confined modes in dielectric photonic nanostructures.

DOI: 10.1103/PhysRevB.87.155314 PACS number(s): 79.20.Uv, 42.70.Qs, 42.82.Et

I. INTRODUCTION

Tiny confined optical modes of high-quality Q factor are fundamental building blocks in the field of photonics. Among other properties, their capability to enhance light-matter interaction is important for the development of ultrahigh sensitive sensors and quantum optical devices.[1] Imaging the electromagnetic field of such modes is intrinsically difficult as the main part of the information about the field is stored in evanescent contributions. Although techniques such as near-field scanning optical microscopy (SNOM) are able to investigate these evanescent contributions[2] they are restricted to surface imaging. Here, we demonstrate the imaging of high-Q modes confined in dielectric planar photonic crystal (PhC) nanocavities using high-energy resolution electron energy-loss spectroscopy. We retrieve spatially resolved information about the intensity distribution and the local state of polarization of the optical field at the dense core of the cavity, paving the way for a highly resolved tomography of photonic nanocavities.

Electron energy-loss spectroscopy (EELS) acquired during scanning transmission electron microscopy (STEM) can obtain the electron energy-loss distribution with a sub-nm or even atomic spatial resolution, depending on the associated physical loss mechanism. Such a technique has recently been intensively used in the low energy-loss part of the spectrum for investigating electromagnetic modes confined in plasmonic nanostructures.[3,4] The coupling of the moving charge with the local optical density of states induces the electron energy loss, which is known as the Vavilov-Cherenkov (VC) effect in a homogeneous and transparent dielectric medium.[5] Imaging of local fields with the electron beam (e-beam) in metallic[6,7] and dielectric[8] structures has been demonstrated with a spatial resolution of a few nm, surpassing by several order of magnitude the sub-μm diffraction limit intrinsic to conventional optical far-field techniques. In contrast to the previous studies, here we investigate a high-Q point defect mode in a subwavelength cavity. A particular difference is that we probe the mode inside the solid matrix as opposed to interpreting EELS signal only in the PhC holes.[8] Moreover, we show that the EELS signal is not subject to spurious residual luminescence in contrast to cathodoluminescence.[9]

II. OPTICAL CAVITY PROBED WITH EELS

Among the different types of subwavelength cavities, planar dielectric photonic crystal cavities defined in membranes of subwavelength scale thickness combine the advantage of a large Q factor with a strong confinement of the electromagnetic mode in a volume smaller than the wavelength cube.[10,11] We focus on a so-called L3 photonic crystal cavity that is defined by a line defect of three missing holes inside a triangular lattice of holes (lattice constant $a = 460$ nm). The three first holes located on both sides of the line defect have been slightly laterally shifted away from the core by a length of $(0.17a, 0.07a, 0.05a)$ to optimize the Q factor. As shown in Fig. 1, the pattern of holes is etched in a 220 nm thick silicon membrane that is sufficiently thin to permit the transmission of the 200 keV e-beam. The lithographically prepared membrane was cut out of its substrate by using a focused ion beam, and then rendered as a TEM lamella by attaching it to a TEM grid using ion-beam-deposited amorphous carbon.

The structure was patterned with deep UV lithography on a silicon on insulator (SOI) wafer and designed to operate at a wavelength around 1.5 μm (filling factor $f = 35\%$). Light coupling into the cavity mode is carried out via a side-coupled photonic crystal waveguide located four lines of holes away from the cavity as explained in Ref. 12. The optical scattering spectrum of the cavity reveals a fundamental mode with a quality factor of 17900 after wet etching of the buried 2 μm thick silicon oxide insulator [see Fig. 1(d)]. The theoretical amplitude distribution of the electric field of the fundamental transverse electric (TE) cavity mode [Fig. 1(b)] exhibits a symmetric pattern of several maxima, whose corresponding local vector fields [Fig. 1(c)] are oriented along the y axis for the ones in the middle of the line defect and along the x axis

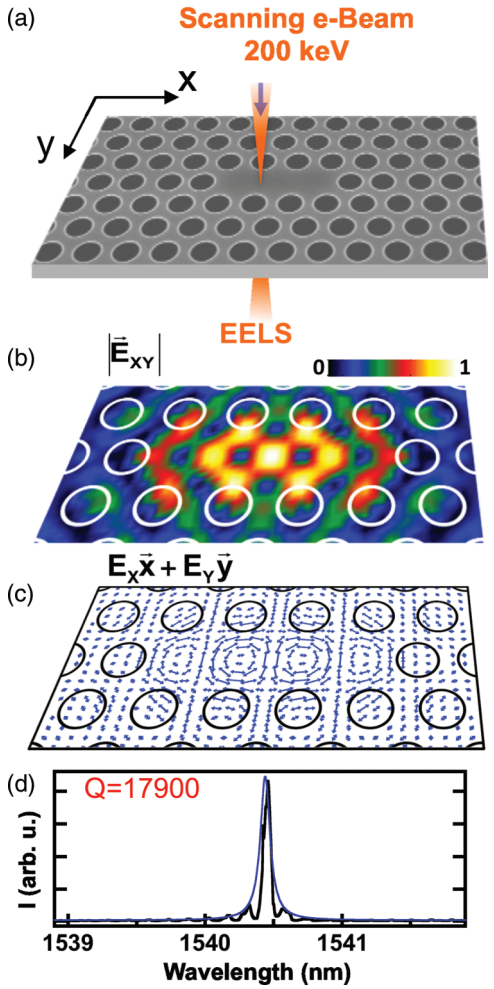

FIG. 1. (Color online) (a) Perspective view of a scanning electron micrograph of the investigated L3 photonic crystal cavity. Spacing between the center of the holes: 460 nm along the x axis. (b) Theoretical amplitude of the electric field $|E_{xy}|$ of the fundamental confined mode of the L3 cavity and (c) local orientation. The calculations are based on a two-dimensional (2D) plane wave expansion calculation with an effective index of the slab $n_{\text{eff}} = 2.77$, i.e., the effective index of the fundamental guided mode (Ref. 12). (d) Optical scattering spectrum of the L3 cavity mode with the corresponding Lorentzian fit (blue line). The spectrum was measured from the surface-emitted light from the membrane.

for the ones at the side of the line defect. Such a vacuum field will impact the energy of moving charged particles through the cavity, as now explained by the following equations.

III. DESCRIPTION OF THE EELS TECHNIQUE

An electron moving at a constant velocity induces a Lorentz force whose work is given by

$$\Delta E = \int_0^{+\infty} \hbar\omega \Gamma_{\text{EELS}}(\omega) d\omega = e \int_{t_1}^{t_2} \vec{v} \cdot \vec{E}(\vec{r}_e(t),t) dt, \quad (1)$$

where $\Gamma_{\text{EELS}}(\omega)$ is the energy-loss probability at the angular frequency ω and $\vec{E}(\vec{r}_e(t),t)$ the electric field at the particle position at time t. The time integral is performed along the trajectory $\vec{r}_e(t)$ of the charge e, which is given by $\vec{r}_e(t) = \vec{R}_0 + z(t)\vec{z}$ for a straight trajectory. From (1), the energy-loss probability can be related to the harmonic components of the electric field

$$\Gamma_{\text{EELS}}(\vec{R}_0,\omega) = \frac{e}{\pi\hbar\omega} \int_{t_1}^{t_2} Re\{\vec{v} \cdot \vec{E}(\vec{r}_e(t),\omega) e^{-i\omega t}\} dt. \quad (2)$$

EELS allows measurement of the energy distribution of the electron beam source after transmission through the investigated medium. The scalar product in Eq. (2) highlights that this technique is sensitive to the state of polarization of the excited field along the electron beam path. For a given orientation of the e-beam relative to the normal of the planar structure, the EELS signal recorded at a particular energy $\hbar\omega$ provides the summation of the local electric fields excited along the e-beam path. In particular, the energy loss is expected to vanish if the excited field stays orthogonal to the electron velocity over the entire e-beam path. To test this, high-energy resolution STEM EELS experiments were performed using the Sub-Electronvolt Sub-Angström Microscope (SESAM) from Carl Zeiss in the Stuttgart Center for Electron Microscopy. The monochromated e-beam allowed recording of the low energy-loss part of the EELS spectra with an energy resolution given by the full-width half-maximum of the zero-loss peak of ~100–110 meV. Such an energy resolution, which corresponds to a resolving power of the instrument of 2×10^6 for a 200 keV e-beam, currently represents the state of the art for electron spectroscopy. The 200 keV energy of the e-beam provides fast enough electrons to promote energy loss via radiation effects. STEM-EELS spectrum images of the optical cavity were taken using a nominal 8 nm spot size, reducing under sampling of the μm-scale optical cavity compared to the best spatial resolution offered by the instrument, using an 11 meV/pixel dispersion on the energy-loss axis. A convergence semiangle of the electron probe of about 15 mrad and a collection semiangle on the EELS spectrometer of about 3 mrad were used, ensuring a forward-scattering condition consistent with the theoretical aspects of this analysis. Spectrum image data were treated as described in Appendix B.

IV. EXPERIMENTAL RESULTS

EELS spectra for the cavity sample and a reference planar slab are shown in Fig. 2. For a homogeneous planar waveguide perpendicular to the e-beam the transverse magnetic (TM) polarized modes are the unique modes that contribute to the electron energy loss via the VC effect. In particular, the presence of TM guided modes is highlighted by the superposition of energy bands due to the continuous nature of their dispersion curves, as investigated in Ref. 13, and seen clearly here for the dark curve of the planar slab in Fig. 2. The onset of the presence of the first TM guided mode is revealed by a significant step in the EELS spectrum. In contrast to guided modes, a confined cavity mode produces a clear peak in the EELS spectrum. Such a spectral feature appears in Fig. 2 at an energy-loss value consistent with the expected frequency of the fundamental TE cavity mode when the PhC membrane is tilted towards the e-beam (see the part of the red curve in the gray area, note also that a higher-order mode of the cavity can be resolved at 1.06 eV). Critically, while this spectral feature is small, maps of the integrated EELS intensity at

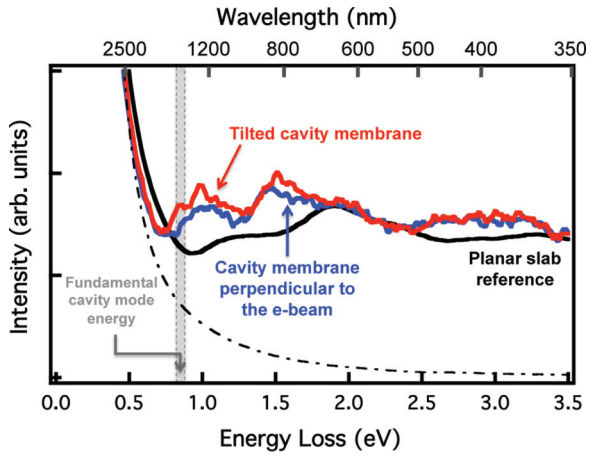

FIG. 2. (Color online) Experimental electron energy-loss spectra for a reference crystalline Si slab waveguide with a nominal thickness of 220 nm (dark curve), a planar photonic crystal cavity at normal incidence from the electron beam (blue curve), and tilted towards the e-beam (red curve). The latter two spectra result from a summation of the EELS intensity over a square area of 150 nm × 150 nm that is located at the center of the L3 photonic crystal cavity defect, as defined by the white dashed square in Fig. 3. The gray window highlights the energy position of the fundamental cavity mode within the EELS energy resolution. Dash-dot line: reference zero-loss peak in the vacuum.

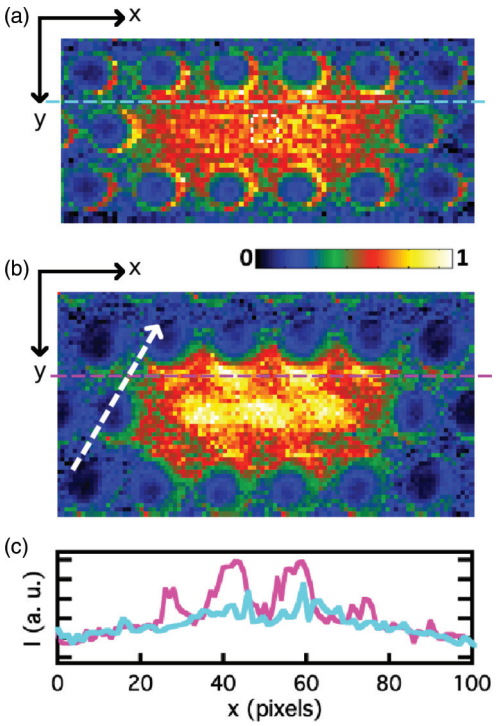

FIG. 3. (Color online) STEM-EELS images of the planar photonic crystal cavity at the cavity mode resonance, built from the integrated intensity of the EELS spectra at the cavity mode energy (integrating between 0.77–0.88 eV as shown by the energy range in gray on Fig. 2). (a) is at normal incidence to the e-beam while (b) is tilted towards the e-beam by a rotation of +26 degrees around the axis represented by the white dashed arrow. Lattice constant $a = 460$ nm along the x axis. The color scales of (a) and (b) are scaled identically relative to the intensity of the normalized zero-loss signal. The EELS signal has been normalized by the integrated zero-loss intensity as described in Appendix C. (c) EELS intensity profiles taken along the cyan and magenta dashed lines in (a) and (b), respectively.

the peak position show that it is unambiguously attributed to the fundamental cavity mode [Fig. 3(b)]. Further, the map in Fig. 3(a) and relevant spectrum in Fig. 2 show that it vanishes for an excitation at normal incidence (blue curve). Not only is this in agreement with the TE polarization of the mode, it is in contrast with cathodoluminescence experiments reported in Ref. 9. This indicates that those results were not produced by a pure VC effect but rather from the interaction of light, incoherently emitted by the residual luminescence of the SiN material, with the PhC structure.

In Fig. 3(b) the membrane is counterclockwise rotated by +26 degrees around the axis represented by the white dashed arrow. It implies a rotation of +12 degrees around the x axis and another one of +23 degrees around the y axis. A clear signature of the high-Q cavity mode is revealed by the presence of several intensity maxima when the photonic crystal membrane is tilted towards the e-beam. The location of these maxima is consistent with the theoretical intensity distribution of the electric field modulus presented in Fig. 1(b). The spacing between the different peaks is 30 times smaller than the resolution given by the optical diffraction limit at 1.5 μm. The three maxima that are located in the middle of the line defect correspond to an electric field orientation along the y axis [see Fig. 1(c)] and, therefore, contribute to the electron energy loss if the membrane is rotated around the x axis. The intensity hot spots at the border of the cavity line defect are associated with a local electric field polarized along the x axis and appear for a rotation around the y axis. Importantly, the intensity profile measured in Fig. 3(b) is not directly proportional to the envelope of the resonant cavity mode, as discussed in Appendix A.

At normal incidence [Fig. 3(a)] the hot spots of the cavity mode disappear. In this orientation a signal is however present in the core of the cavity L3 defect. It is two times larger than the background signal in the bulk PhC [see Fig. 3(c)]. Such a signal is unexpected within the framework of a 2D plane wave expansion (PWE) model where the PhC structure is supposed to be invariant along the z axis.[14] The transverse electric TE and transverse magnetic TM modes that form a complete orthonormal set of eigenstates are here defined by the vectors $(E_x, E_y, E_z = 0, H_x = 0, H_y = 0, H_z)$ and $(E_x = 0, E_y = 0, E_z, H_x, H_y, H_z = 0)$, respectively. Note that for planar guided modes the invariance is within the x-y plane and, for modes propagating along the x axis, the TE and TM modes are defined by $(E_x = 0, E_y, E_z = 0, H_x, H_y = 0, H_z)$ and $(E_x, E_y = 0, E_z, H_x = 0, H_y, H_z = 0)$, respectively. The presence of the planar waveguide breaks the invariance along the z axis, which induces a hybridization between the TE and TM modes. In general, the PWE model is nevertheless a good approximation and the modes can be classified as quasi-TE or quasi-TM. In the current case, the hybridization of the confined PWE-based TE cavity mode with the extended TM modes generates an E_z field component for the actual cavity mode. The presence of this component can be probed by the electron beam as revealed by Fig. 3(a). Its spatial distribution is localized within the cavity defect as the

hybridization coupling constant involves the component of the PWE-based TE cavity mode. Besides, the slight conic shape of the hole also breaks the invariance along the z axis and, as a result, also contributes to the presence of the E_z field component.[15]

Such a conic shape of the holes is, in addition, responsible for the asymmetry of the in-plane $|E_{xy}|$ intensity distribution that is observed near the border holes of the cavity defect in Fig. 3(b). A cross section would reveal that, because such holes are not invariant along the z axis, once the PhC structure is tilted e-beams that are located at symmetrical but opposite positions from the center of the cavity experience different dielectric environments when taking paths near the border of the holes. This then produces different energy losses that do not reflect the symmetry of the pattern.

V. DISCUSSION

We now extend the above analysis by suggesting the use of this technique to obtain the complete 3D information about the optical scattering properties and the confined modes of such structures. This would be done by determining the excited electric field at particular local positions. Such a field can be expressed with the electric field Green's tensor $\overleftrightarrow{G}$ of the scattering medium from Maxwell's equations, as follows:

$$\vec{E}(\vec{r}_e,\omega) = i\omega\mu_0 \int_V \overleftrightarrow{G}(\vec{r}_e,\vec{r}\,';\omega)\cdot\vec{J}(\vec{r}\,',\omega)d^3\vec{r}\,' \qquad (3)$$

with $\vec{J}$ the current density. The experimental determination of the local electric field excited by a known current density gives access to the Green's tensor, i.e., it provides complete 3D information about the scattering properties and the confined modes of the structures. One ideal approach to retrieve the Green's tensor would consist in controlling, in a noninvasive way, the 3D position, the orientation, and the cyclic frequency ω of an elementary dipole placed inside the photonic structure. In practice, however, the required experiment is challenging. EELS spectroscopy offers an alternative to this local dipole excitation approach by probing the medium with a line current $\vec{J}(\vec{r}\,';\omega) = -e\vec{v}/v\delta_{\vec{R}_0}e^{i\omega z'/v}$. At a given position $(\vec{R}_0,z)$ the harmonic electric field can be expressed as

$$\vec{E}(\vec{R}_0,z,\omega) = \frac{e}{v}i\omega\mu_0\int_\ell \overleftrightarrow{G}(\vec{R}_0,z,\vec{R}_0,z';\omega)\cdot\vec{v}e^{i\omega z'/v}dz'. \quad (4)$$

The integration is performed along the ℓ trajectory of the electron. In contrast to the case of the dipolar excitation, the determination of the induced field at the electron position involves a Fourier transform of the Green's tensor along the electron trajectory.[16] Besides, this equation reveals that the local induced field depends on the orientation of the sample. As a result, if the induced field is known for several orientations at several positions, the Green's tensor can be deduced by inverting a system formed by equations similar to (4).

Thus, from the above, recording STEM-EELS data with different sample orientations brings the supplementary inputs that are necessary to determine the excited electric field at a particular local position of the path. This creates the possibility of 3D tomographic analyses of the electric field in optical cavities in a way not possible with the surface imaging nature of SNOM. The correlation between the spatial EELS data and the mode envelope is more complicated than the "projection rule" that is conventionally required for tomographic reconstructions (see Appendix A). However, given that conventional tomographic data acquisition and analysis are well established in electron, neutron, or x-ray microscopy,[17] this more complicated reconstruction should be feasible. Since we have also experimentally confirmed the required sensitivity of the EELS technique to both the intensity distribution and the local polarization of the electric field in a high-Q optical cavity, this paves the way for a highly spatially resolved and noninvasive reconstruction technique of confined resonant modes in dense dielectric photonic structures.

ACKNOWLEDGMENTS

The authors acknowledge the ePIXfab platform in IMEC for the fabrication of the PhC samples and the Stuttgart Center for Electron Microscopy at the MPI for Intelligent Systems for providing access to the Sub-Electronvolt Sub-Angström Microscope (SESAM). This work was supported by the Swiss NCCR-Quantum Photonics, the Swiss National Science Foundation (SNSF) (Project No. 200021-124413), and the COST action MP0702. ESTEEM (Enabling Science and Technology through European Electron Microscopy) supported the transnational microscopy access to the SESAM. Christoph T. Koch at Ulm University and Guillaume Lucas of CIME, EPFL are thanked for help with scripting in DigitalMicrograph.

APPENDIX A: THEORETICAL DESCRIPTION OF THE ELECTRON ENERGY LOSS VIA THE INTERACTION WITH A CAVITY MODE

The aim of this theoretical Appendix is to investigate the relation between the energy-loss probability that is measured with EELS spectroscopy and the envelope ϕ_0 of a TE cavity mode. As discussed in the body of the paper, the electron energy-loss probability of an electron is given by Eq. (2) and the induced electric field is completely determined by the electric Dyadic Green's function and the exciting current density, as revealed by Eq. (3). To highlight the salient features of the physical process we restrict the theory to a scalar model. Within this approximation the Green's function can be written

$$G(\vec{r}_e,\vec{r}\,') = \sum_n \frac{\phi_n(\vec{r}_e)\phi_n^*(\vec{r}\,')}{\omega-\lambda_n}, \qquad (A1)$$

where $\{\phi_n\}$ is the orthonormal set of the eigenmodes of the operator that describes the electromagnetic medium and λ_n are the associated eigenvalues. If we consider only the fundamental TE cavity mode with ϕ_0 being the amplitude of the mode envelope, the scalar Green's function can be further simplified as

$$G(\vec{r}_e,\vec{r}\,') \approx \frac{\phi_0(\vec{r}_e)\phi_0^*(\vec{r}\,')}{\omega-\lambda_0} = \frac{\phi_0(\vec{r}_e)\phi_0^*(\vec{r}\,')}{\omega-\omega_0+i\frac{1}{\tau_c}}, \qquad (A2)$$

where ω_0 is the resonant frequency and τ_c the lifetime of the cavity mode. The parameter τ_c takes into account the dissipation of the cavity mode and is determined from the linewidth of the Lorentzian function that describes the cavity mode spectrum.

First we consider the case of a dipole excitation at $\vec{r}_e$. The current density is given by $J(\vec{r}',\omega) = p\delta(\vec{r}_e)$, where p is the dipole moment. It follows that

$$E(\vec{r}_e,\omega) = i\omega\mu_0 \frac{\phi_0(\vec{r}_e)\phi_0^*(\vec{r}_e)}{\omega-\omega_0+i\frac{1}{\tau_c}} p \tag{A3}$$

and the dissipated power $P(\omega) = \frac{\omega}{2}\mathrm{Im}(p^*E)$ can then be expressed by

$$P(\omega) = \mu_0|p|^2 \frac{\frac{\omega^2}{2}}{(\omega-\omega_0)^2+\left(\frac{1}{\tau_c}\right)^2}|\phi_0(\vec{r}_e)|^2. \tag{A4}$$

As a result, the intensity profile of the cavity mode can be determined in the 3D space. However, it requires addressing a single well-defined dipole inside the cavity.

In the case of an e-beam current along the (Oz'_e) axis and located at $\vec{R}'_e$, the current density is given by $J(\vec{R}',z';\omega) = -e\delta(\vec{R}'-\vec{R}'_e)e^{i\omega(z'-z'_e)/v}$ where v is the amplitude of the electron velocity and $\vec{r}\,' = \vec{R}' + \vec{z}'$. The scalar field is then given by

$$E(\vec{r}_e,\omega) = -i\mu_0 e \frac{\omega}{\omega-\omega_0+i\frac{1}{\tau_c}}\phi_0(\vec{r}_e) \times \int_{-\infty}^{+\infty} \phi_0^*(\vec{R}'_e,z')e^{i\omega(z'-z'_e)/v}dz'. \tag{A5}$$

From this expression we can deduce the electron energy-loss probability, i.e., the quantity that is experimentally accessible

$$\Gamma_{\mathrm{EELS}}(\vec{R}_e,\omega) = -\frac{\mu_0 e^2}{\pi\hbar\omega}\mathrm{Im}\left\{\frac{\omega}{\omega-\omega_0+i\frac{1}{\tau_c}}\int_{-\infty}^{+\infty}\phi_0(\vec{R}_e,z_e) \times e^{-i\omega t}\int_{-\infty}^{+\infty}\phi_0^*(\vec{R}'_e,z')e^{i\omega(z'-z'_e)/v}dz'dt\right\} v\cos(\theta_e). \tag{A6}$$

In this last equation, we have taken into account the angle θ_e between the electric field at $\vec{r}_e$ and the electron velocity. We suppose that the orientation of the electric field stays constant along the path, i.e., θ_e is considered constant within the current scalar approximation. As $t = (z_e - z'_e)/v$, the two sums are complex conjugates and it follows that

$$\Gamma_{\mathrm{EELS}}(\vec{R}_e,\omega) = \frac{\mu_0 e^2}{\pi\hbar}\cos(\theta_e)\frac{\tau_c^{-1}}{(\omega-\omega_0)^2+\tau_c^{-2}} \times \left|\int_{-\infty}^{+\infty}\phi_0(\vec{R}_e,z_e)e^{-i\omega z_e/v}dz_e\right|^2. \tag{A7}$$

Such an equation constitutes the main result of the model: for one given orientation of the beam, the spatially resolved EELS data provide an image of the square modulus of the Fourier transform of the mode envelope along the beam direction. Note that no general threshold condition on the velocity amplitude is expected for the onset of the coupling to optical radiation in the case of a charged particle moving in PhC structures.[18,19] This contrasts with the Vavilov-Cherenkov effect observed in a homogeneous dielectric and transparent medium.

APPENDIX B: DISCUSSION ON THE NEED FOR NORMALIZATION OF EELS SPECTRA

In each STEM-EELS spectrum image, postprocessing was used to align the EELS spectra by zero-loss peak position on the energy-loss axis, in order to account for fluctuations in zero energy-loss position that primarily result from minor instabilities in high tension. Because of multiple inelastic scattering from plasmons and ionization excitations that occur in the bulk, it is apparent that a map of the raw radiative excitation intensity in the EELS spectrum across a pattern of bulk and holes does not properly reflect the nature of this excitation. To recover the true radiative excitation distribution, each EELS spectrum in the data volume was therefore normalized by the intensity (integrated area) of its zero-loss peak of elastically scattered electrons (see Appendix C for detailed explanation). The zero-loss component was identified by precisely fitting the peaks with zero-loss spectra recorded in vacuum under the same experimental conditions.[20–22]

For the above processes to work it is important to record the entire zero-loss peak in each spectrum without saturating the spectrometer camera during data acquisition. Since the radiative signal scales with zero-loss intensity, and since zero-loss intensity is significantly diminished in the bulk compared to vacuum (see Appendix C), given the constraint of a uniform spectral exposure time during spectrum image data acquisition this consequently limits signal-to-noise for the relatively weak radiative excitations, particularly in the bulk. The diminished zero-loss intensity in bulk compared to vacuum is demonstrated in Fig. 4. In future it is planned to overcome this signal acquisition limitation with use of the latest instrumental developments, specifically use of a

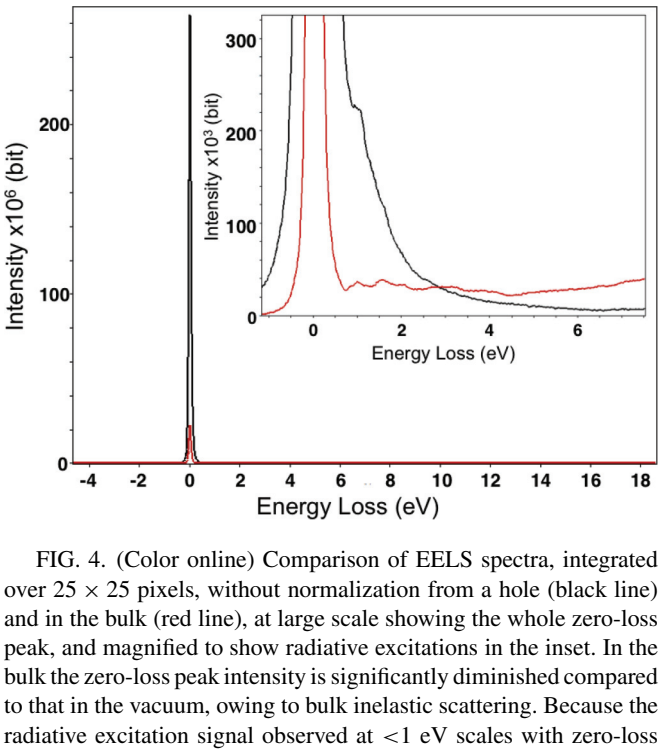

FIG. 4. (Color online) Comparison of EELS spectra, integrated over 25 × 25 pixels, without normalization from a hole (black line) and in the bulk (red line), at large scale showing the whole zero-loss peak, and magnified to show radiative excitations in the inset. In the bulk the zero-loss peak intensity is significantly diminished compared to that in the vacuum, owing to bulk inelastic scattering. Because the radiative excitation signal observed at <1 eV scales with zero-loss intensity, and because the zero-loss signal is far stronger in the hole where there is no bulk inelastic scattering, in this raw data the radiative excitation appears much stronger in the vacuum than in the bulk.

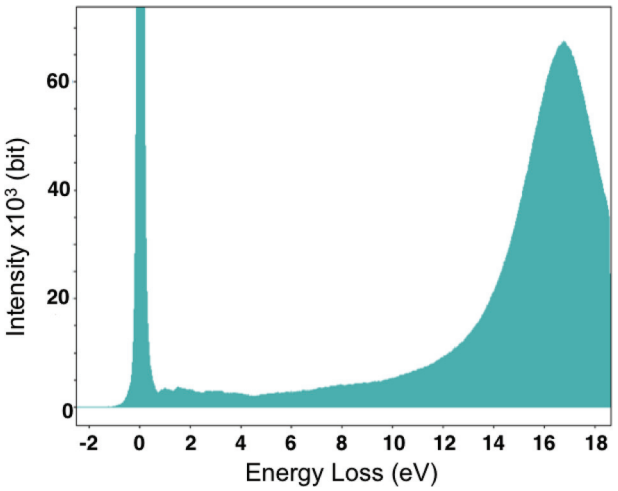

FIG. 5. (Color online) EELS spectrum integrated over 25 × 25 pixels, extracted from the optical cavity excitation, with the e-beam penetrating the bulk. The bulk plasmon excitation peaking at ∼16.7 eV energy loss is far more intense than the radiative excitation at <1 eV energy loss.

dual-channel EELS spectrometer to allow the near simultaneous two spectra per spatial pixel, one with a short temporal acquisition time including the full zero-loss signal, the other with a longer acquisition time with the zero-loss peak displaced off the spectrometer.

APPENDIX C: DISCUSSION ON THE NEED FOR NORMALIZATION OF EELS SPECTRA

In this section we describe the reasons behind the use of a normalization procedure on the EELS spectra. Planar PhCs consist of patterns of holes made in a membrane of 200–300 nm thickness. Furthermore, here we study an optical cavity whose core consists of missing holes, for which data must be taken with the e-beam penetrating the Si bulk. In contrast, previously published studies of electric fields in PhCs have focused on spectra taken for the e-beam in the vacuum, at the center or near the edges of the holes; a so-called aloof e-beam geometry (e.g., see Refs. 8 and 23). Since the e-beam does not penetrate the bulk in this latter geometry, energy loss of the transmitted electrons results only from radiative and surface plasmon excitations. However, in the geometry studied here with the e-beam penetrating the bulk,

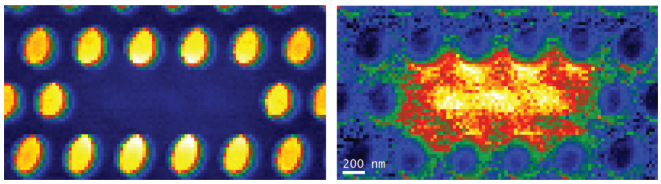

FIG. 6. (Color online) Comparison of the same energy-loss maps for the optical cavity integrated over the same energy window, before (left) and after (right) normalization of the EELS spectra by zero-loss intensity.

there is also energy loss of the transmitted electrons from bulk plasmon excitations and inner shell ionization of atoms in the matrix (which together we refer to as bulk inelastic scattering). Because of the significant thickness of the Si membrane, ∼90% of the incident electrons suffer such bulk inelastic scattering. This presents a problem for mapping the intensity distribution from the radiative excitations across a pattern of holes and bulk, as now explained.

The transmitted electrons all have sufficiently similar speeds to suffer equivalent radiative excitations. However, when the e-beam penetrates the bulk, in the EELS spectrum the radiative excitation signal is convoluted with the energy loss from the bulk inelastic scattering. Compared to the plasmon excitations it is a weak signal (see Fig. 5), and thus the only reliably observed radiative signal is that associated with electrons that are otherwise solely elastically scattered, what we can term quasielastically scattered electrons. Because the intensity of these quasielastically scattered electrons is much stronger in the vacuum (where there is no bulk inelastic scattering) relative to the bulk (see Fig. 4), their intensity in maps from raw spectral data is correspondingly enhanced in the vacuum, but in a manner that is not representative of the radiative excitation effect alone. However, assuming that the radiative excitation signal in any one place is directly proportional to the intensity of elastically scattered electrons in the zero-loss peak, it is apparent that the representative radiative excitation distribution can be retrieved by normalizing each spectrum by its zero-loss peak intensity.[24] As shown in Fig. 6, this normalization makes a dramatic difference to the visibility of the radiative excitation in the optical cavity, and will play an essential role in future research aimed towards further analyzing the 3D distribution of electric fields in optical structures.

*nicolas.le.thomas@intec.ugent.be
†Present address: Photonic Research Group, Department of Information Technology, Ghent University-IMEC, Sint-Pietersnieuwstraat 41, B-9000 Ghent, Belgium

[1]K. J. Vahala, Nature (London) **424**, 839 (2003).
[2]L. Novotny and B. Hecht, *Principles of Nano-Optics*, 1st ed. (Cambridge University Press, Cambridge, 2006).
[3]F. J. Garcia de Abajo, Rev. Mod. Phys. **82**, 209 (2010).
[4]A. Yurtsever, R. M. van der Veen, and A. H. Zewail, Science **335**, 59 (2012).
[5]V. L. Ginzburg, Phys. Usp. **39**, 973 (1996).
[6]J. Nelayah, M. Kociak, O. Stéphan, F. J. Garca de Abajo, M. Tencé, L. Henrard, D. Taverna, I. Pastoriza-Santos, L. M. Liz-Marzán, and C. Colliex, Nature Phys. **3**, 348 (2007).
[7]R. Vogelgesang and A. Dmitriev, Analyst **135**, 1175 (2010).
[8]J. J. Cha, Z. Yu, E. Smith, M. Couillard, S. Fan, and D. A. Muller, Phys. Rev. B **81**, 113102 (2010).
[9]R. Sapienza, T. Coenen, J. Renger, M. Kuttge, N. F. van Hulst, and A. Polman, Nature Mater. **11**, 781 (2012).

[10]Y. Akahane, T. Asano, B. S. Song, and S. Noda, Nature (London) **425**, 944 (2003).
[11]E. Kuramochi, M. Notomi, S. Mitsugi, and T. Watanabe, Appl. Phys. Lett. **88**, 041112 (2006).
[12]N. Le Thomas and R. Houdré, Phys. Rev. B **84**, 035320 (2011).
[13]A. Yurtsever, M. Couillard, and D. A. Muller, Phys. Rev. Lett. **100**, 217402 (2008).
[14]M. Plihal and A. A. Maradudin, Phys. Rev. B **44**, 8565 (1991).
[15]Y. Tanaka, T. Asano, R. Hatsuta, and S. Noda, Appl. Phys. Lett. **88**, 011112 (2006).
[16]U. Hohenester, H. Ditlbacher, and J. R. Krenn, Phys. Rev. Lett. **103**, 106801 (2009).
[17]P. A. Midgley, E. P. W. Ward, A. B. Hungría, and J. M. Thomas, Chem. Soc. Rev. **36**, 1477 (2007).
[18]C. Luo, M. Ibanescu, S. G. Johnson, and J. D. Joannopoulos, Science **299**, 368 (2003).
[19]C. Kremers, D. N. Chigrin, and J. Kroha, Phys. Rev. A **79**, 013829 (2009).
[20]B. W. Reed and M. Sarikaya, Ultramicroscopy **93**, 25 (2002).
[21]D. T. L. Alexander, P. A. Crozier, and J. R. Anderson, Science **321**, 833 (2008).
[22]For zero-loss processing Digital Micograph scripts please contact guillaume.lucas@epfl.ch.
[23]F. J. García de Abajo, A. G. Pattantyus-Abraham, N. Zabala, A. Rivacoba, M. O. Wolf, and P. M. Echenique, Phys. Rev. Lett. **91**, 143902 (2003).
[24]Christoph T. Koch and F. J. Javier García de Abajo (private communication).